Electron heat flux and whistler instability in the Earth's magnetosheath

Citation for the original published paper (version of record):
Svenningsson, I., Yordanova, E., Khotyaintsev, Y. et al (2026). Electron heat flux and whistler instability in the Earth's magnetosheath. Physical Review E, 113(6).
http://dx.doi.org/10.1103/hd9q-t7z8

Letter

Electron heat flux and whistler instability in the Earth's magnetosheath

Ida Svenningsson,[1,2,3,*] Emiliya Yordanova,[1] Yuri V. Khotyaintsev,[1,2] Mats André,[1] Giulia Cozzani,[4] Alexandros Chasapis,[5] and Steven J. Schwartz[5,6]

[1] *Swedish Institute of Space Physics, Uppsala 751 21, Sweden*
[2] *Department of Physics and Astronomy, Uppsala University, Uppsala 751 20, Sweden*
[3] *Department of Physics and Astronomy, Chalmers University of Technology, Göteborg 412 96, Sweden*
[4] *Laboratory of Physics and Chemistry of the Environment and Space (LPC2E), OSUC, Univ Orleans, CNRS, CNES, 45071 Orleans, France*
[5] *Laboratory for Atmospheric and Space Physics, University of Colorado, Boulder, Colorado 80303, USA*
[6] *Department of Physics, Imperial College London, London SW7 2AZ, United Kingdom*

(Received 27 October 2025; accepted 21 May 2026; published 15 June 2026)

Despite heat flux's role in regulating energy conversion in collisionless plasmas, its properties and evolution in the magnetosheath downstream of the Earth's bow shock are scarcely explored. We use Magnetospheric Multiscale *in situ* measurements to quantify and characterize the electron heat flux in the magnetosheath. We find that the heat flux is shaped by the magnetosheath magnetic field as it drapes around the magnetosphere. While it is affected by solar wind upstream conditions and increases with magnetic field strength, it is not substantially changed by local magnetosheath processes. Also, the heat flux is limited by whistler instability thresholds.

DOI: 10.1103/hd9q-t7z8

Introduction. Electrons control the thermal energy transfer in plasmas due to their low mass compared to ions [1], making the electron heat flux central to the total energy budget. In the weakly collisional regime, the electron heat flux is suppressed below the collisional Spitzer-Härm [2] prediction, as observed in the solar wind [3] and the intracluster medium of galaxy clusters [4,5]. Instead, wave-particle interactions are believed to suppress the heat flux on ion and electron kinetic scales in heliospheric [6] and astrophysical [7] plasmas.

The electron heat flux $\boldsymbol{q}_e$ is defined as the third-order moment of the electron velocity distribution function (eVDF):

$$\boldsymbol{q}_e = \frac{m_e}{2}\int f_e(\boldsymbol{v})|\boldsymbol{w}|^2\boldsymbol{w}\,d^3v, \tag{1}$$

where $f_e(\boldsymbol{v})$ is the eVDF, $\boldsymbol{w} = \boldsymbol{v} - \boldsymbol{V}_e$ is the velocity $\boldsymbol{v}$ in the electron bulk flow ($\boldsymbol{V}_e$) frame, and m_e is the electron mass. The heat flux can be calculated directly from the eVDF in spacecraft observations [3,6,8–10]. However, since $\boldsymbol{q}_e$ is sensitive to noise related to low count rates, detailed calculations of $\boldsymbol{q}_e$ from spacecraft data have mostly been done for case studies [9,10]. In the solar wind (SW), $\boldsymbol{q}_e$ can be obtained by fitting the eVDF core, halo, and strahl components as drifting bi-Maxwellians [11,12]. In hybrid simulations, $\boldsymbol{q}_e$ can be inferred through thermodynamic closures such as Landau-fluid-type closures [13,14]. Data-driven closures using machine learning [15] and sparse regression [16] have also been suggested. However, it remains a challenge to estimate $\boldsymbol{q}_e$ in spacecraft data, notably when the eVDF is strongly non-Maxwellian [17].

Collisionless shocks are associated with strong particle acceleration and heating in various astrophysical environments such as supernova remnants [18], interplanetary shocks [19,20], and planetary bow shocks [21,22]. Among these, the Earth's bow shock (BS) is uniquely accessible to *in situ* measurements of electron dynamics. At the BS, electrons are accelerated and heated adiabatically, creating separated hot and cold components. Additionally, nonadiabatic effects due to, e.g., wave-particle interactions [23] become significant at high Mach numbers in the de Hoffmann-Teller reference frame [24]. This heating gives the eVDF in the downstream magnetosheath (MSH) region a "flat top" shape at low energies [25], significantly different from the eVDF in the SW. The heating is also expected to change $\boldsymbol{q}_e$, but the resulting change in $\boldsymbol{q}_e$ across the BS is not known. Moreover, $\boldsymbol{q}_e$ may be altered locally in the MSH by reconnecting current sheets [26–31], wave-particle interactions [32–36], or magnetic reconnection at the magnetopause (MP) [10,37]. The relevant space mission allowing the access to electron scales is the Magnetospheric Multiscale (MMS) mission [38], equipped with state-of-the-art instrumentation, permitting the estimation of higher-order moments of the eVDF, such as the heat flux.

In the SW, $\boldsymbol{q}_e$ can be regulated by different wave instabilities, of which the whistler wave dominates for $\beta_{e\parallel} \gtrsim 0.1$ [11], where $\beta_{e\parallel} = 2\mu_0 n_e T_{e\parallel}/B^2$ and n_e and $T_{e\parallel}$ are the electron density and temperature parallel to the magnetic field $\boldsymbol{B}$, and $B = |\boldsymbol{B}|$. Heat flux instabilities can generate both parallel-propagating [11] and highly oblique [39] whistler waves, the interplay of which

*Contact author: ida.svenningsson@chalmers.se

results in a heat flux reduction [40]. However, the regulation of $\boldsymbol{q}_e$ in the MSH, a compressible, high-β region in contrast to the SW [41,42], remains unknown. Previous analyses also assumed a SW-type eVDF. Studying the MSH allows us to investigate the more general applicability of the scenario where the heat flux is regulated by these instabilities.

Whistler waves are regularly observed in the MSH. While the most commonly proposed generation mechanism requires a high electron temperature anisotropy [43], whistler waves are not typically associated with the high electron temperature anisotropy required to trigger waves [33]. This can be partly explained by highly non-Maxwellian eVDFs [32,44,45]. Therefore, heat flux instabilities should be investigated as alternative candidates for whistler wave generation.

To explore the poorly understood nature of electron heat flux downstream of collisionless shocks, we use measurements from the MMS mission to statistically study the electron heat flux in the MSH and its evolution from the BS to the MP. We also explore the effect of local heat flux regulation by investigating the relationship with whistler waves.

Data and methods. We use MMS data from the 2023 *unbiased magnetosheath campaign* [32], where 3 min of burst-mode data were sampled every 9 min providing 14 full inbound MSH crossings with a total of 13.9 h of data. The fluxgate magnetometer (FGM) [46] provides the magnetic field vector $\boldsymbol{B}$ and the fast plasma investigation [47] instruments give the full three-dimensional eVDF every 30 ms. We use the highest-resolution burst-mode data to avoid effects of lossy compression of fast-mode data [48]. We preprocess the electron heat flux to remove nonphysical noise originating from low-counting statistics. The noise removal algorithm, described in the Supplemental Material [49], involves removing extreme values, correcting for the spacecraft spin tone, and smoothing the signal with a 1-s window.

Results. Figure 1 shows one of the 3-min intervals from the MSH. Figures 1(a)–1(d) show $\boldsymbol{B}$, n_e, $\boldsymbol{V}_e$, and parallel and perpendicular temperatures ($T_{e\parallel}$, $T_{e\perp}$ with respect to $\boldsymbol{B}$), respectively. In the first half of the interval, B and n_e display an anticorrelation typical of mirror-mode waves common in the quasiperpendicular MSH configuration [50], where the mirror modes modulate $T_{e\perp}$ [51]. Figure 1(e) shows the electron heat flux $\boldsymbol{q}_e$ in field-aligned coordinates. The parallel component $q_{e\parallel}$ dominates, consistent with approximately gyrotropic observed eVDFs. We note that $\boldsymbol{q}_e$ changes direction in the vicinity of a sharp $\boldsymbol{B}$ variation at 13:20:50. Figures 1(f) and 1(g) show the two-dimensional (2D) eVDFs $f_e(v_\parallel, v_{\perp 1})$ at two times: at 13:19:35, there is a parallel heat flux, and at 13:20:33, the heat flux is antiparallel. The associated asymmetry is visible in f_e, especially in Fig. 1(g) where f_e is skewed towards negative $v_\parallel$ at high energies. Thus, the heat flux can vary locally in the MSH, and its behavior is not directly predictable from other moments (n_e, $\boldsymbol{V}_e$, $T_{e\parallel}$, and $T_{e\perp}$).

We now investigate whether local variations in the heat flux such as the one shown in Fig. 1(e) accumulate to a significant change across the MSH. We quantify the large-scale heat flux with $\langle q_e \rangle_{3\text{min}}$, the mean magnitude of $\boldsymbol{q}_e$ in each 3-min burst interval. Figure 2(a) shows the locations of MMS in the geocentric solar ecliptic (GSE) XY plane with color and arrows indicating $\langle q_e \rangle_{3\text{min}}$ and the mean vectors $\langle \boldsymbol{q}_e \rangle_{3\text{min}}$, respectively. The solid and dotted curves show models of the BS and MP,

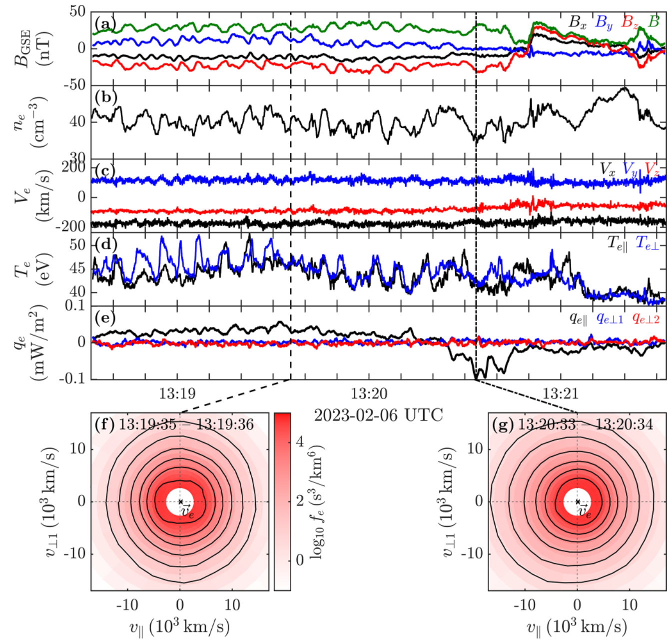

FIG. 1. Three-minute interval from the MSH. MMS measurements of the magnetic field $\boldsymbol{B}$ (a) and the electron moments: (b) density n_e, (c) bulk velocity $\boldsymbol{V}_e$, (d) temperatures parallel ($T_{e\parallel}$) and perpendicular ($T_{e\perp}$) to $\boldsymbol{B}$, and (e) heat flux $\boldsymbol{q}_e$ in field-aligned components. Panels (f) and (g) show 2D eVDFs $f_e(v_\parallel, v_{\perp 1})$ (averaged over 1 second) taken from 13:19:35 and 13:20:33, respectively, where $v_\parallel = \boldsymbol{v} \cdot \hat{\boldsymbol{b}}$ and $v_{\perp 1} = \boldsymbol{v} \cdot [\hat{\boldsymbol{b}} \times (\hat{\boldsymbol{e}} \times \hat{\boldsymbol{b}})]$, and $\hat{\boldsymbol{b}} = \boldsymbol{B}/B$ and $\hat{\boldsymbol{e}} = \boldsymbol{E}/E$ are the magnetic and electric field directions, respectively.

respectively, based on average SW conditions (retrieved from the OMNI database [52]) during the considered intervals, and the variation of their locations is indicated in gray (see details in Ref. [53]).The $\boldsymbol{q}_e$ direction is tied to the magnetic field lines which are approximately aligned with the BS surface since the MSH is observed in a quasiperpendicular configuration [33]. In each orbit, $\langle q_e \rangle_{3\text{min}}$ does not change within the MSH with a few exceptions (e.g., $\langle q_e \rangle_{3\text{min}}$ increasing with BS distance in orbit 1 and the rotation in orbit 7). The SW conditions, such as the interplanetary magnetic field direction $\hat{\boldsymbol{b}}_{\text{SW}}$, are mostly stable during the individual orbits, while in orbits where $\hat{\boldsymbol{b}}_{\text{SW}}$ rotates this is accompanied with rotation in $\boldsymbol{q}_e$ (see Supplemental Material [49]). For two orbits, 7 and 14, the MSH is highly compressed, with MSH measurements well within the average MP. This is due to a high-speed stream (orbit 7) and a coronal mass ejection (orbit 14). In both cases, $\langle q_e \rangle_{3\text{min}}$ is 3–10 times higher than that in the other orbits.

Figure 2(b) shows that $\langle q_e \rangle_{3\text{min}}$ increases with the local MSH magnetic field strength B_{MSH}. The same dependence is seen with respect to B_{SW} (color scale) and with the SW dynamic pressure (see Supplemental Material [49]). The fit (black curve) based on the orbit-averages reveals that q_e is approximately proportional to B_{MSH}. Interestingly, this scaling with B is similar to previous observations in the SW at $1-5$ AU (red circles, Scime *et al.*, S94 [6]).

In Fig. 2(c), we study the $\boldsymbol{q}_e$ evolution across the MSH using $\langle q_e \rangle_{3\text{min}}$ normalized to the mean value in each orbit. We estimate the location relative to the MP and the BS with the fractional distance $d_{\text{MP}-\text{BS}}$, defined so that $d_{\text{MP}-\text{BS}} = 0$ at the

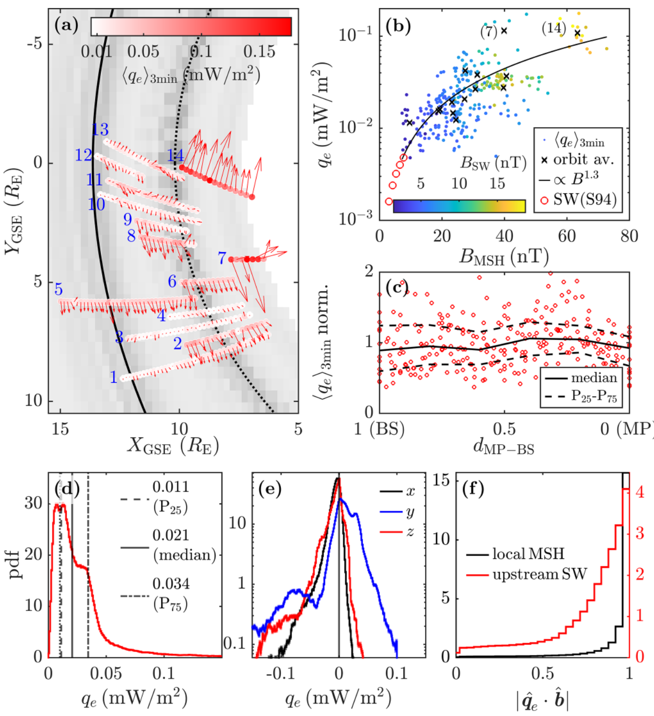

FIG. 2. Electron heat flux across the MSH. (a) MMS location in each 3-min burst interval in the GSE XY plane [$Z_{\mathrm{GSE}} \sim (-7, -5)R_{\mathrm{E}}$]. Color indicates $\langle q_e \rangle_{3\mathrm{min}}$ and arrows indicate the projected $\langle \boldsymbol{q}_e \rangle_{3\mathrm{min}}$. Orbits are labeled chronologically 1–14 with blue numbers. (b) $\langle q_e \rangle_{3\mathrm{min}}$ versus B_{MSH}; the color scale shows B_{SW}. The black curve shows the fit $q_e \approx 3 \times 10^{-4} B^{1.3}$ based on the orbit-average values (black crosses). Red circles show approximate values of B and q_e from the SW, obtained by reading off the axes in Fig. 13 in Scime *et al.* (S94) [6]. (c) Evolution of $\langle q_e \rangle_{3\mathrm{min}}$ (normalized to the mean in each orbit) with the fractional distance $d_{\mathrm{MP-BS}}$. The solid curve shows the median in bins of width 0.2, and the dashed curves show the 25th and 75th percentiles in the bins. Individual orbits are shown in red. (d) Overall q_e in the MSH; median value shown with a solid curve, and 25th and 75th percentiles shown in dashed and dash-dotted curves. The dotted line indicates the estimated uncertainty 0.01 mW/m^2 (see Supplemental Material [49]). (e) GSE components of $\boldsymbol{q}_e$. (f) Alignment of $\hat{\boldsymbol{q}}_e = \boldsymbol{q}_e / q_e$ with the local magnetic field direction $\hat{\boldsymbol{b}}_{\mathrm{MSH}} = \boldsymbol{B}_{\mathrm{MSH}}/B_{\mathrm{MSH}}$ (black curve) and the upstream solar wind magnetic field direction $\hat{\boldsymbol{b}}_{\mathrm{SW}} = \boldsymbol{B}_{\mathrm{SW}}/B_{\mathrm{SW}}$ (red curve).

MP and $d_{\mathrm{MP-BS}} = 1$ at the BS [53,54]. We show the individual orbits in red and the black curves show the median (solid curves), 25th and 75th percentiles (dashed curves) in bins of width $d_{\mathrm{MP-BS}} = 0.2$. While there is a large variation across different orbits, there is no clear evolution of the normalized $\langle q_e \rangle_{3\mathrm{min}}$ with $d_{\mathrm{MP-BS}}$, indicating that the electron heat flux is not significantly created or destroyed in the MSH.

Figures 2(d)–2(f) show histograms of $\boldsymbol{q}_e$ without time averaging, i.e., obtained from the entire dataset, corresponding to 1 671 203 eVDFs. The median q_e is 0.021 mW/m^2 and 50% of the data are within 0.012 and 0.035 mW/m^2 [see Fig. 2(d)]. This is slightly higher than reported values of 0.005–0.01 mW/m^2 in the SW at 1 AU [6,55,56]. The x component is negative [$q_{ex} < 0$; black in Fig. 2(e)] similar to the anti-sunward strahl in the SW. Its southward direction ($q_{ez} < 0$; red curve) indicates that the heat flux is directed

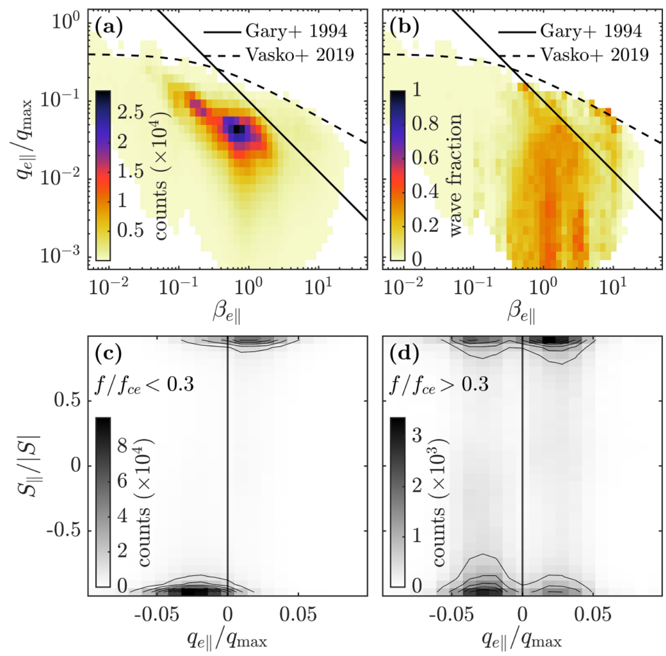

FIG. 3. Whistler heat flux instabilities. (a) 2D histogram of $|q_{e\parallel}|/q_{\max}$ and $\beta_{e\parallel}$ with each count corresponding to one 30-ms electron measurement. (b) Whistler wave occurrence in the $\beta_{e\parallel} - |q_{e\parallel}|/q_{\max}$ parameter space. We show two whistler instability thresholds: the parallel heat flux instability (solid curve: Gary+ 1994 [11]: $|q_{e\parallel}|/q_{\max} = 0.10\beta_{e\parallel}^{-0.90}$ for a growth rate $\gamma = 10^{-3}\Omega_p$, where Ω_p is the angular proton cyclotron frequency) and the oblique heat flux fan instability (dashed curve: Vasko+ 2019 [39]: $|q_{e\parallel}|/q_{\max} = 0.20[\beta_{e\parallel} + 0.25]^{-0.50}$). (c) Normalized Poynting flux $S_\parallel/|S|$ of low-frequency whistler waves ($f/f_{ce} < 0.3$) versus $q_{e\parallel}/q_{\max}$. (d) Same as panel (c) but for high-frequency ($f/f_{ce} > 0.3$) whistler waves.

around the magnetosphere since MMS is located at $Z_{\mathrm{GSE}} < 0$ during the entire dataset (not shown). As expected for approximately gyrotropic distributions, $\boldsymbol{q}_e$ is aligned with the local magnetic field [$|\hat{\boldsymbol{q}}_e \cdot \hat{\boldsymbol{b}}_{\mathrm{MSH}}| \approx 1$, black in Fig. 2(f)]. Moreover, since $|\hat{\boldsymbol{q}}_e \cdot \hat{\boldsymbol{b}}_{\mathrm{SW}}|$ is predominantly 1 [Fig. 2(f)] the heat flux likely follows the magnetic field draping around the magnetosphere (see also Supplemental Material [49]).

To understand how the heat flux is regulated in the magnetosheath, we compare the heat flux distribution to instability thresholds for the whistler heat flux instability, which is the most likely instability since $\beta_{e\parallel} \gtrsim 0.1$ in our dataset [11]. Figure 3(a) shows the $\beta_{e\parallel} - |q_{e\parallel}|/q_{\max}$ parameter space, where $q_{\max} = \frac{3}{2} m_e n_e v_{\mathrm{th}}^3$ is the free-streaming heat flux [3] and $v_{\mathrm{th}} = \sqrt{T_e/m_e}$ is the thermal speed. We show the instability threshold for parallel propagating waves (solid curves) [11] and oblique waves (dashed curves) [39], The bulk of the data is bounded by the parallel threshold and the oblique threshold provides an upper boundary on the distribution. This suggests that the whistler instability regulates the heat flux in the MSH.

To further explore the role of whistler instabilities, we compare the heat flux to whistler wave packets analyzed previously in Ref. [33]. The wave packets are mainly found parallel-propagating with respect to $\boldsymbol{B}$ and appear in two frequency bands; the majority with $f/f_{ce} \in (0.1, 0.3)$ and a smaller population with $f/f_{ce} \in (0.3, 0.6)$, where

$f_{ce} = eB/(2\pi m_e)$ is the electron cyclotron frequency [33]. In Fig. 3(b) we show the fraction of data points in the MSH during which whistler wave packets are observed. Whistler activity is mainly observed for $\beta_{e\parallel} > 0.1$ as noted in Ref. [33]. Apart from an increased wave activity at the oblique instability threshold (dashed curve) for $\beta_{e\parallel} \approx 10$, whistler activity does not correlate with a high heat flux close to the instability thresholds. However, the whistler wave distribution follows the parallel whistler instability threshold (solid curve), suggesting that there is a connection between heat flux and whistler waves.

In general, due to the asymmetry of the eVDF, whistler waves produced by the heat flux instability propagate along the magnetic field in the same direction as the heat flux [57], while the temperature anisotropy instability generates both parallel and antiparallel waves. Therefore, we investigate the wave propagation direction using the Poynting flux $\boldsymbol{S}$, which is parallel to the group velocity. Figure 3(c) shows $S_\parallel/|\boldsymbol{S}|$, the normalized parallel Poynting flux with respect to $\boldsymbol{B}$, versus $q_{e\parallel}/q_{\max}$, for low-frequency ($f/f_{ce} < 0.3$) whistler wave packets, i.e., where the majority of the observed waves are found. The clustering in the top right and bottom left corners indicates that the wave packets are predominantly aligned with the heat flux, consistent with the whistler heat flux instability. On the other hand, the propagation of high-frequency waves [$f/f_{ce} > 0.3$; Fig. 3(d)] has less alignment with $q_{e\parallel}$.

Discussion. In this Letter, we statistically analyze the electron heat flux across the MSH, from the BS to the MP. We find that the heat flux in the MSH shares traits of the heat flux in the upstream SW, as it is mainly field aligned and has an anti-sunward component. Some properties are altered; most notably, the direction follows the field line draping around the magnetosphere and the magnitude is higher than typical values in the solar wind, especially when the magnetic field is strong. Due to the order-of-magnitude variations between different orbits, the upstream conditions likely impact the heat flux downstream of the bow shock. Importantly, both cases of highly compressed MSH show significantly higher values compared to other orbits.

We find that q_e increases proportionally to the local magnetic field strength $B_{\rm MSH}$ and the upstream $B_{\rm SW}$. A correlation between q_e and $B_{\rm SW}$ has been observed in the SW at 1–5 AU [6]; however, this was also a radial effect as both q_e and B decrease with distance from the sun. In this work, the reason for the proportionality is not clear. Possibly the correlation exists in the SW even at 1 AU. Moreover, considering the high q_e in the MSH compared to that in the SW, it seems that q_e increases at the BS. With the present dataset, we cannot determine the relative impacts of upstream conditions and shock acceleration processes. This requires larger datasets as well as continuous $\boldsymbol{q}_e$ measurements from the SW to the MSH.

The magnitude of the electron heat flux remains relatively steady within the MSH during individual orbits. Although it can vary locally, the cumulative effect of potential sources and sinks does not globally affect the heat flux magnitude. One potential source for heat flux is magnetic reconnection at the MP [10]. However, we do not observe an increase of heat flux close to this boundary ($d_{\rm MP-BS} \approx 0$). This suggests that the heat flux created at the MP remains in the vicinity of the MP.

The heat flux is limited by the parallel [11] and oblique [39] whistler instability thresholds. Since the MSH whistlers tend to propagate quasiparallel to $\boldsymbol{B}$ [33], the parallel instability is expected to dominate. However, given the upper bound by the oblique threshold, there may be impact from both instabilities. We find that there is no increase in whistler wave activity when the heat flux is close to the instability thresholds, indicating that the heat flux is not the major source of waves. As the same instabilities bound the heat flux in the SW [8,11,58], the fact that the heat flux is constrained by these instability thresholds can be a remainder of SW dynamics, where the heat flux has already been actively regulated by the whistler instability.

On the other hand, a possible whistler-heat flux instability is supported by the alignment between low-frequency ($f/f_{ce} < 0.3$) whistlers and the heat flux direction. Also, the wave occurrence is constrained by the parallel whistler instability, similarly to what has been observed in the SW [58]. Thus, this instability cannot be ruled out. One possibility is that the asymmetric features typical of the heat flux instability exist in the whistler-resonant parts of the eVDF (satisfying the first-order cyclotron resonance condition, typically a few times the thermal energy [33]). Thus, the heat flux calculated from the entire distribution may not necessarily predict an instability [45]. Also, high (low) electron temperature anisotropies can trigger (quench) the onset of the whistler heat flux instability [59,60], which could affect the spread in wave occurrence. Considering the agreement with instability thresholds and the directional alignment, we suggest that the heat flux whistler instabilities play a role in the MSH.

For a reliable estimation of the electron heat flux, the analysis presented here required removing noise and nonphysical data spikes and correcting for a spin signal (see Supplemental Material [49]). Previously, the heat flux had been obtained from the eVDF with another method [10], by restricting the energy range and estimating the errors from Poisson statistics. However, this is more suitable for case studies due to the heavy processing of the full eVDF at each time step. Our approach provides an alternative better suited for statistical studies when a large amount of data needs to be processed.

Conclusions. The electron heat flux is important for understanding energy conversion in space, astrophysical, and laboratory plasma. Using 13.9 h of burst-mode data from the magnetospheric multiscale mission, we statistically study the electron heat flux downstream of the Earth's bow shock, how it evolves inside the magnetosheath, and its potential regulation by whistler instabilities. We find that the magnetosheath electron heat flux is slightly higher than that in the solar wind at 1 AU and that it drapes around the magnetosphere following the magnetic field lines. Its magnitude varies with upstream solar wind conditions and increases with magnetic field strength. However, local processes in the magnetosheath do not substantially change the heat flux during propagation from the bow shock to the magnetopause. The heat flux is constrained by the parallel and oblique whistler instability thresholds, and the alignment of low-frequency whistler wave propagation with the heat flux direction further supports a connection between electron heat flux and whistler waves.

Being a statistical study of electron heat flux downstream of the Earth's bow shock, our findings should be instructive when analyzing heat conduction downstream of astrophysical shocks such as supernova remnants [61–63], as well as other collisionless, high-β plasmas which are not accessible for *in situ* measurements, including the interstellar medium [64] and black hole accretion disks [65,66]. Our results thus provide a valuable contribution to the understanding the global energy budget in the MSH and can also serve as a reference for modeling the electron heat flux in high-β, compressible plasmas.

Acknowledgments. MMS data are available at the MMS Science Data Center [67]. Data analysis was performed using the irfu-matlab package [68]. We thank the MMS team and instrument PIs for data access and support. We thank Heli Hietala, Istvan Pusztai and Tünde Fülöp for valuable input. We acknowledge support from the Swedish Research Council under Grant No. 2016-0550 and the Swedish National Space Agency under Grants No. 158/16 and No. 192/20. This research was supported by the International Space Science Institute (ISSI) in Bern, through the ISSI International Team project No. 23-588 ("Unveiling Energy Conversion and Dissipation in Non-Equilibrium Space Plasmas"). The work was supported by the Knut and Alice Wallenberg Foundation. The work of G.C. is supported by the Integration Fellowship of Le Studium Loire Valley Institute for Advanced Studies.

Data availability. The data that support the findings of this article are openly available [67].

[1] D. Verscharen, R. T. Wicks, O. Alexandrova, R. Bruno, D. Burgess, C. H. K. Chen, R. D'Amicis, J. De Keyser, T. D. De Wit, L. Franci, J. He, P. Henri, S. Kasahara, Y. Khotyaintsev, K. G. Klein, B. Lavraud, B. A. Maruca, M. Maksimovic, F. Plaschke, S. Poedts, *et al.*, A case for electron-astrophysics, Exp. Astron. **54**, 473 (2022).

[2] L. Spitzer and R. Härm, Transport phenomena in a completely ionized gas, Phys. Rev. **89**, 977 (1953).

[3] S. D. Bale, M. Pulupa, C. Salem, C. H. K. Chen, and E. Quataert, Electron heat conduction in the solar wind: Transition from Spitzer-Härm to the collisionless limit, Astrophys. J. **769**, L22 (2013).

[4] J. Binney and L. L. Cowie, X-ray emission from M87—A pressure confined cooling atmosphere surrounding a low mass galaxy, Astrophys. J. **247**, 464 (1981).

[5] M. Markevitch, P. Mazzotta, A. Vikhlinin, D. Burke, Y. Butt, L. David, H. Donnelly, W. R. Forman, D. Harris, D.-W. Kim, S. Virani, and J. Vrtilek, *Chandra* temperature map of A754 and constraints on thermal conduction, Astrophys. J. **586**, L19 (2003).

[6] E. E. Scime, S. J. Bame, W. C. Feldman, S. P. Gary, J. L. Phillips, and A. Balogh, Regulation of the solar wind electron heat flux from 1 to 5 AU: Ulysses observations, J. Geophys. Res.: Space Phys. **99**, 23401 (1994).

[7] G. T. Roberg-Clark, J. F. Drake, M. Swisdak, and C. S. Reynolds, Wave generation and heat flux suppression in astrophysical plasma systems, Astrophys. J. **867**, 154 (2018).

[8] J. S. Halekas, P. L. Whittlesey, D. E. Larson, D. McGinnis, S. D. Bale, M. Berthomier, A. W. Case, B. D. G. Chandran, J. C. Kasper, K. G. Klein, K. E. Korreck, R. Livi, R. J. MacDowall, M. Maksimovic, D. M. Malaspina, L. Matteini, M. P. Pulupa, and M. L. Stevens, Electron heat flux in the near-Sun environment, Astron. Astrophys. **650**, A15 (2021).

[9] J. T. Coburn, D. Verscharen, C. J. Owen, M. Maksimovic, T. S. Horbury, C. H. K. Chen, F. Guo, X. Fu, J. Liu, J. B. Abraham, G. Nicolaou, M. E. Innocenti, A. Micera, and V. K. Jagarlamudi, The regulation of the solar wind electron heat flux by wave–particle interactions, Astrophys. J. **964**, 100 (2024).

[10] D. J. Gershman, L. Chen, A. Le, J. Shuster, J. C. Dorelli, J. Ng,B. Giles, A. F. Viñas, R. Torbert, and J. L. Burch, The evolution of parallel electron temperature in magnetospheric reconnection inflows, Geophys. Res. Lett. **51**, e2024GL109783 (2024).

[11] S. P. Gary, E. E. Scime, J. L. Phillips, and W. C. Feldman, The whistler heat flux instability: Threshold conditions in the solar wind, J. Geophys. Res. **99**, 23391 (1994).

[12] S. P. Gary, R. M. Skoug, and W. Daughton, Electron heat flux constraints in the solar wind, Phys. Plasmas **6**, 2607 (1999).

[13] F. Finelli, S. S. Cerri, F. Califano, F. Pucci, D. Laveder, G. Lapenta, and T. Passot, Bridging hybrid- and full-kinetic models with Landau-fluid electrons, Astron. Astrophys. **653**, A156 (2021).

[14] P. L. Sulem and T. Passot, Landau fluid closures with nonlinear large-scale finite Larmor radius corrections for collisionless plasmas, J. Plasma Phys. **81**, 325810103 (2015).

[15] Z. Huang, C. Dong, and L. Wang, Machine-learning heat flux closure for multi-moment fluid modeling of nonlinear Landau damping, Proc. Natl. Acad. Sci. USA **122**, e2419073122 (2025).

[16] E. R. Ingelsten, M. C. McGrae-Menge, E. P. Alves, and I. Pusztai, Data-driven discovery of a heat flux closure for electrostatic plasma phenomena, J. Plasma Phys. **91**, E64 (2025).

[17] D. B. Graham, Y. V. Khotyaintsev, M. André, A. Vaivads, A. Chasapis, W. H. Matthaeus, A. Retinò, F. Valentini, and D. J. Gershman, Non-Maxwellianity of electron distributions near earth's magnetopause, J. Geophys. Res.: Space Phys. **126**, e2021JA029260 (2021).

[18] M. Pohl and J. A. Esposito, Electron acceleration in supernova remnants and diffuse gamma rays above 1 GeV, Astrophys. J. **507**, 327 (1998).

[19] S. W. Kahler, Solar sources of heliospheric energetic electron events—Shocks or flares? Space Sci. Rev. **129**, 359 (2007).

[20] L. Yang, L. Wang, G. Li, R. F. Wimmer-Schweingruber, J. He, C. Tu, H. Tian, and S. D. Bale, The strongest acceleration of >40 keV electrons by ICME-driven shocks at 1 au, Astrophys. J. **853**, 89 (2018).

[21] J. L. Phillips, S. J. Bame, M. F. Thomsen, B. E. Goldstein, and E. J. Smith, Ulysses plasma observations in the Jovian magnetosheath, J. Geophys. Res.: Space Phys. **98**, 21189 (1993).

[22] G. Andreone, J. S. Halekas, D. L. Mitchell, C. Mazelle, and J. Gruesbeck, Properties of electron distributions in the

Martian space environment, J. Geophys. Res.: Space Phys. **127**, e2021JA029404 (2022).

[23] T. Amano, M. Masuda, M. Oka, N. Kitamura, O. Le Contel, and D. J. Gershman, Statistical analysis of high-frequency whistler waves at Earth's bow shock: Further support for stochastic shock drift acceleration, Phys. Plasmas **31**, 042903 (2024).

[24] A. Lalti, Y. V. Khotyaintsev, and D. B. Graham, Adiabatic and non-adiabatic electron heating at quasi-perpendicular collisionless shocks, Geophys. Res. Lett. **51**, e2024GL112547 (2024).

[25] W. C. Feldman, R. C. Anderson, S. J. Bame, S. P. Gary, J. T. Gosling, D. J. McComas, M. F. Thomsen, G. Paschmann, and M. M. Hoppe, Electron velocity distributions near the Earth's bow shock, J. Geophys. Res.: Space Phys. **88**, 96 (1983).

[26] A. Retinò, D. Sundkvist, A. Vaivads, F. Mozer, M. André, and C. J. Owen, In situ evidence of magnetic reconnection in turbulent plasma, Nat. Phys. **3**, 235 (2007).

[27] E. Yordanova, Z. Vörös, A. Varsani, D. B. Graham, C. Norgren, Y. V. Khotyaintsev, A. Vaivads, E. Eriksson, R. Nakamura, P.-A. Lindqvist, G. Marklund, R. E. Ergun, W. Magnes, W. Baumjohann, D. Fischer, F. Plaschke, Y. Narita, C. T. Russell, R. J. Strangeway, O. Le Contel, *et al.*, Electron scale structures and magnetic reconnection signatures in the turbulent magnetosheath, Geophys. Res. Lett. **43**, 5969 (2016).

[28] Z. Vörös, E. Yordanova, A. Varsani, K. J. Genestreti, Y. V. Khotyaintsev, W. Li, D. B. Graham, C. Norgren, R. Nakamura, Y. Narita, F. Plaschke, W. Magnes, W. Baumjohann, D. Fischer, A. Vaivads, E. Eriksson, P. Lindqvist, G. Marklund, R. E. Ergun, M. Leitner, *et al.*, MMS observation of magnetic reconnection in the turbulent magnetosheath, J. Geophys. Res.: Space Phys. **122**, 11442 (2017).

[29] T. D. Phan, J. P. Eastwood, M. A. Shay, J. F. Drake, B. U. Ö. Sonnerup, M. Fujimoto, P. A. Cassak, M. Øieroset, J. L. Burch, R. B. Torbert, A. C. Rager, J. C. Dorelli, D. J. Gershman, C. Pollock, P. S. Pyakurel, C. C. Haggerty, Y. Khotyaintsev, B. Lavraud, Y. Saito, M. Oka, *et al.*, Electron magnetic reconnection without ion coupling in Earth's turbulent magnetosheath, Nature (London) **557**, 202 (2018).

[30] J. E. Stawarz, J. P. Eastwood, T. D. Phan, I. L. Gingell, M. A. Shay, J. L. Burch, R. E. Ergun, B. L. Giles, D. J. Gershman, O. L. Contel, P.-A. Lindqvist, C. T. Russell, R. J. Strangeway, R. B. Torbert, M. R. Argall, D. Fischer, W. Magnes, and L. Franci, Properties of the turbulence associated with electron-only magnetic reconnection in earth's magnetosheath, Astrophys. J. Lett. **877**, L37 (2019).

[31] J. E. Stawarz, J. P. Eastwood, T. D. Phan, I. L. Gingell, P. S. Pyakurel, M. A. Shay, S. L. Robertson, C. T. Russell, and O. Le Contel, Turbulence-driven magnetic reconnection and the magnetic correlation length: Observations from magnetospheric multiscale in Earth's magnetosheath, Phys. Plasmas **29**, 012302 (2022).

[32] I. Svenningsson, E. Yordanova, G. Cozzani, Y. V. Khotyaintsev, and M. André, Kinetic generation of whistler waves in the turbulent magnetosheath, Geophys. Res. Lett. **49**, e2022GL099065 (2022).

[33] I. Svenningsson, E. Yordanova, Y. V. Khotyaintsev, M. André, G. Cozzani, and K. Steinvall, Whistler waves in the quasi-parallel and quasi-perpendicular magnetosheath, J. Geophys. Res.: Space Phys. **129**, e2024JA032661 (2024).

[34] C. H. K. Chen, K. G. Klein, and G. G. Howes, Evidence for electron Landau damping in space plasma turbulence, Nat. Commun. **10**, 740 (2019).

[35] A. S. Afshari, G. G. Howes, J. R. Shuster, K. G. Klein, D. McGinnis, M. M. Martinović, S. A. Boardsen, C. R. Brown, R. Huang, D. P. Hartley, and C. A. Kletzing, Direct observation of ion cyclotron damping of turbulence in Earth's magnetosheath plasma, Nat. Commun. **15**, 7870 (2024).

[36] H. Breuillard, O. Le Contel, T. Chust, M. Berthomier, A. Retino, D. L. Turner, R. Nakamura, W. Baumjohann, G. Cozzani, F. Catapano, A. Alexandrova, L. Mirioni, D. B. Graham, M. R. Argall, D. Fischer, F. D. Wilder, D. J. Gershman, A. Varsani, P. Lindqvist, Y. V. Khotyaintsev, *et al.*, The properties of lion roars and electron dynamics in mirror mode waves observed by the magnetospheric multiscale mission, J. Geophys. Res.: Space Phys. **123**, 93 (2018).

[37] W. Gonzalez and E. Parker, Editors, *Magnetic Reconnection: Concepts and Applications*, Astrophysics and Space Science Library (Springer, Cham, 2016), Vol. 427.

[38] J. L. Burch, T. E. Moore, R. B. Torbert, and B. L. Giles, Magnetospheric multiscale overview and science objectives, Space Sci. Rev. **199**, 5 (2016).

[39] I. Y. Vasko, V. Krasnoselskikh, Y. Tong, S. D. Bale, J. W. Bonnell, and F. S. Mozer, Whistler fan instability driven by strahl electrons in the solar wind, Astrophys. J. Lett. **871**, L29 (2019).

[40] A. Micera, A. N. Zhukov, R. A. López, M. E. Innocenti, M. Lazar, E. Boella, and G. Lapenta, Particle-in-cell simulation of whistler heat-flux instabilities in the solar wind: Heat-flux regulation and electron halo formation, Astrophys. J. Lett. **903**, L23 (2020).

[41] S. Y. Huang, L. Z. Hadid, F. Sahraoui, Z. G. Yuan, and X. H. Deng, On the existence of the Kolmogorov inertial range in the terrestrial magnetosheath turbulence, Astrophys. J. **836**, L10 (2017).

[42] E. Yordanova, Z. Vörös, S. Raptis, and T. Karlsson, Current sheet statistics in the magnetosheath, Front. Astron. Space Sci. **7**, 2 (2020).

[43] S. P. Gary and J. Wang, Whistler instability: Electron anisotropy upper bound, J. Geophys. Res.: Space Phys. **101**, 10749 (1996).

[44] N. Kitamura, Y. Omura, S. Nakamura, T. Amano, S. A. Boardsen, N. Ahmadi, O. Le Contel, P. Lindqvist, R. E. Ergun, Y. Saito, S. Yokota, D. J. Gershman, W. R. Paterson, C. J. Pollock, B. L. Giles, C. T. Russell, R. J. Strangeway, and J. L. Burch, Observations of the source region of whistler mode waves in magnetosheath mirror structures, J. Geophys. Res.: Space Phys. **125**, e2019JA027488 (2020).

[45] B. Page, I. Y. Vasko, A. V. Artemyev, and S. D. Bale, Generation of high-frequency whistler waves in the Earth's quasi-perpendicular bow shock, Astrophys. J. Lett. **919**, L17 (2021).

[46] C. T. Russell, B. J. Anderson, W. Baumjohann, K. R. Bromund, D. Dearborn, D. Fischer, G. Le, H. K. Leinweber, D. Leneman, W. Magnes, J. D. Means, M. B. Moldwin, R. Nakamura, D. Pierce, F. Plaschke, K. M. Rowe, J. A. Slavin, R. J. Strangeway, R. Torbert, C. Hagen, *et al.*, The magnetospheric multiscale magnetometers, Space Sci. Rev. **199**, 189 (2016).

[47] C. Pollock, T. Moore, A. Jacques, J. Burch, U. Gliese, Y. Saito, T. Omoto, L. Avanov, A. Barrie, V. Coffey, J. Dorelli, D. Gershman, B. Giles, T. Rosnack, C. Salo, S. Yokota, M. Adrian,

C. Aoustin, C. Auletti, S. Aung, *et al.*, Fast plasma investigation for magnetospheric multiscale, Space Sci. Rev. **199**, 331 (2016).
[48] A. C. Barrie, D. L. Smith, S. R. Elkington, Z. Sternovsky, D. Silva, B. L. Giles, and C. Schiff, Wavelet compression performance of MMS/FPI plasma count data with plasma environment, Earth Space Sci. **6**, 116 (2019).
[49] See Supplemental Material at http://link.aps.org/supplemental/10.1103/hd9q-t7z8 for description of the heat flux noise removal method and heat flux dependence on local MSH and upstream SW parameters, which includes Refs. [52,53,69].
[50] A. P. Dimmock, A. Osmane, T. I. Pulkkinen, and K. Nykyri, A statistical study of the dawn-dusk asymmetry of ion temperature anisotropy and mirror mode occurrence in the terrestrial dayside magnetosheath using THEMIS data, J. Geophys. Res.: Space Phys. **120**, 5489 (2015).
[51] S. T. Yao, Q. Q. Shi, J. Liu, Z. H. Yao, R. L. Guo, N. Ahmadi, A. W. Degeling, Q. G. Zong, X. G. Wang, A. M. Tian, C. T. Russell, H. S. Fu, Z. Y. Pu, S. Y. Fu, H. Zhang, W. J. Sun, L. Li, C. J. Xiao, Y. Y. Feng, and B. L. Giles, Electron dynamics in magnetosheath mirror-mode structures, J. Geophys. Res.: Space Phys. **123**, 5561 (2018).
[52] N. E. Papitashvili and J. H. King, NASA Space Physics Data Facility, https://doi.org/10.48322/1shr-ht18 (2020).
[53] I. Svenningsson, E. Yordanova, Y. V. Khotyaintsev, M. André, and G. Cozzani, Classifying the magnetosheath using local measurements from MMS, J. Geophys. Res.: Space Phys. **130**, e2024JA033272 (2025).
[54] A. P. Dimmock and K. Nykyri, The statistical mapping of magnetosheath plasma properties based on THEMIS measurements in the magnetosheath interplanetary medium reference frame, J. Geophys. Res.: Space Phys. **118**, 4963 (2013).
[55] C. A. Cattell, B. Short, A. W. Breneman, and P. Grul, Narrowband large amplitude whistler-mode waves in the solar wind and their association with electrons: STEREO waveform capture observations, Astrophys. J. **897**, 126 (2020).
[56] C. S. Salem, M. Pulupa, S. D. Bale, and D. Verscharen, Precision electron measurements in the solar wind at 1 au from NASA's Wind spacecraft, Astron. Astrophys. **675**, A162 (2023).
[57] D. Verscharen, B. D. G. Chandran, E. Boella, J. Halekas, M. E. Innocenti, V. K. Jagarlamudi, A. Micera, V. Pierrard, Š. Štverák, I. Y. Vasko, M. Velli, and P. L. Whittlesey, Electron-driven instabilities in the solar wind, Front. Astron. Space Sci. **9**, 951628 (2022).
[58] C. Cattell, A. Breneman, J. Dombeck, E. Hanson, M. Johnson, J. Halekas, S. D. Bale, T. Dudok De Wit, K. Goetz, K. Goodrich, D. Malaspina, M. Pulupa, T. Case, J. C. Kasper, D. Larson, M. Stevens, and P. Whittlesey, Parker solar probe evidence for the absence of whistlers close to the sun to scatter strahl and to regulate heat flux, Astrophys. J. Lett. **924**, L33 (2022).
[59] Y. Tong, I. Y. Vasko, M. Pulupa, F. S. Mozer, S. D. Bale, A. V. Artemyev, and V. Krasnoselskikh, Whistler wave generation by halo electrons in the solar wind, Astrophys. J. Lett. **870**, L6 (2019).
[60] Y. Tong, I. Y. Vasko, A. V. Artemyev, S. D. Bale, and F. S. Mozer, Statistical study of whistler waves in the solar wind at 1 au, Astrophys. J. **878**, 41 (2019).
[61] D. Caprioli and A. Spitkovsky, Simulations of ion acceleration at non-relativistic shocks. I. Acceleration efficiency, Astrophys. J. **783**, 91 (2014).
[62] W. Cui and D. P. Cox, Two-temperature models of old supernova remnants with ion and electron thermal conduction, Astrophys. J. **401**, 206 (1992).
[63] T. Inoue, R. Yamazaki, and S.-I. Inutsuka, Turbulence and magnetic field amplification in supernova remnants: Interactions between a strong shock wave and multiphase interstellar medium, Astrophys. J. **695**, 825 (2009).
[64] K. H. Lee and L. C. Lee, Turbulence spectra of electron density and magnetic field fluctuations in the local interstellar medium, Astrophys. J. **904**, 66 (2020).
[65] S. M. Ressler, A. Tchekhovskoy, E. Quataert, M. Chandra, and C. F. Gammie, Electron thermodynamics in GRMHD simulations of low-luminosity black hole accretion, Mon. Not. R. Astron. Soc. **454**, 1848 (2015).
[66] Event Horizon Telescope Collaboration, K. Akiyama, A. Alberdi, W. Alef, J. Carlos Algaba, R. Anantua, K. Asada, R. Azulay, U. Bach, A.-K. Baczko, D. Ball, M. Baloković, J. Barrett, M. Bauböck, B. A. Benson, D. Bintley, L. Blackburn, R. Blundell, K. L. Bouman, G. C. Bower, *et al.*, First sagittarius A* event horizon telescope results. V. Testing astrophysical models of the galactic center black hole, Astrophys. J. Lett. **930**, L16 (2022).
[67] See https://lasp.colorado.edu/mms/sdc/public.
[68] See https://github.com/irfu/irfu-matlab.
[69] E. Kobel and E. O. Flückiger, A model of the steady state magnetic field in the magnetosheath, J. Geophys. Res.: Space Phys. **99**, 23617 (1994).